Classification of Laser Footprint Based on Random Forest in Mountainous Area Using GLAS Full-Waveform Features

Xiangfeng Liu, Xiaodan Liu, Zhenhua Wang, Genghua Huang, and Rong Shu

***Abstract*—Full-waveform spaceborne laser altimeter can provide more characteristic parameters of the laser footprint and rich vertical structure information on the target surface. This technology has the potential for land-cover classification, especially in hard-to-reach mountain areas. Classifying the land types based on the returned waveform can provide a convenient way for the online classification needs and assess the quality of footprint used as the ground control point in photogrammetry. This article presents a random forest (RF) classification using geoscience laser altimeter system waveform, in the west-central Yunnan Province, China. First, an improved threshold wavelet is performed to denoise the waveform, and then Gaussian decomposition is used to extract the typical characteristic features of footprint. Second, an RF algorithm is implemented to clarify the footprints into five types: flat, building, terrace, forest, and mountain. Finally, quantitative analysis is conducted with producer's accuracy (PA), user's accuracy (UA), overall accuracy (OA), precision, recall rate, F1-score, and kappa coefficient to compare the performance of RF with other classifiers, including linear support vector machine (linear-SVM), radial basis function SVM (RBF-SVM), logistic regression (LR), K-nearest neighbor (KNN), and naive Bayes (NB). The results show that all the six methods can accurately classify the flat land with 100.00% PA and UA. The RF also has the best performances in other four land types, with PA and UA of 98.14% and 100.00%, 97.24% and 95.49%, 98.64% and 96.03%, and 94.64% and 100.00%, respectively. The OA, precision, recall, F1-score, and kappa coefficient for the RF are 97.95%, 97.73%, 98.30%, 97.99%, and 0.9737, respectively; while 83.45%, 82.55%, 82.98%, 81.16%, and 0.7765 for NB, which has the worst performance. LR performs better than RBF-SVM, linear-SVM, and KNN. It also observes worse classification accuracy for all methods when the waveforms are more complex.**

***Index Terms*—Classification, full-waveform, Gaussian decomposition, laser footprint, random forest (RF), spaceborne laser altimeter.**

I. Introduction

SPACEBORNE remote sensing has an ability to observe the Earth almost all the time, thus helping to derive more information about the land cover at the global scale. This technology can overcome the disadvantages of traditional field surveying, such as high costs in the time and labor, many hard-to-reach areas, and dependence of subjective judgment [1]. One method of remote sensing is passive optical imagery, which could collect multispectral, hyperspectral, and high-resolution images. However, these image data can only provide the spectral or visual information on object's surface, but not the vertical structural properties. As a result, it is difficult to separate the objects with spectrally similar but structurally different [2], for example, roads and buildings with the same material. Another remote sensing method is active detecting system, including radar and laser technologies. For the radar imagery and radar altimetry, which can penetrate clouds and work in all weather conditions (rain and snowfall) and both day and night-time, with penetration through the vegetation canopy and soil, as well as sensitivity to structure and dielectric properties (liquid vs. frozen water). However, the radar imagery is affected by polarization and backscattering, and the acquisition on textural and spatial features with lower resolution (usually expressed in meters) [3], [4]. The radar altimetry can provide the vertical structural properties, but the measurement and pointing accuracy is worse than the laser (precision with almost twice and increased with the slope) [5]. For the light detection and ranging (LiDAR), it can collect the discrete-return or full-waveform laser echo [6] that directly provide the structural information one object from return pulse with three-dimensional positional measurements [7], [8]. The full-waveform LiDAR has the enhanced ability to capture the time-dependent variation in the echo signal with a specified sampling, and this helps us extract the finer vertical distribution of one geographical object; however, the traditional discrete-return LiDAR only recorded six or fewer echoes along one object's vertical profile typically [9]–[12]. Furthermore, additional features (e.g., metrics in distance) specified by the

---

Manuscript received November 19, 2021; revised January 4, 2022 and January 27, 2022; accepted February 8, 2022. Date of publication February 14, 2022; date of current version March 23, 2022. This work was supported in part by the Shanghai Municipal Science and Technology Major Project under Grant 2019SHZDZX01, in part by the Universities of Shanghai Science and Technology Commission under Grant 19050502100, and in part by the Shanghai Science and Technology Innovation Action Plan Program under Grant 18511102202. *(Corresponding authors: Zhenhua Wang; Rong Shu.)*

Xiangfeng Liu and Genghua Huang are with the Key Laboratory of Space Active Opto-Electronics Technology, Chinese Academy of Sciences (CAS), Shanghai 20083, China, and also with the Shanghai Institute of Technical Physics CAS, Shanghai 20083, China (e-mail: liuxiangfeng@mail.sitp.ac.cn; genghuah@mail.sitp.ac.cn).

Xiaodan Liu and Zhenhua Wang are with the College of Information Technology, Shanghai Ocean University, Shanghai 201306, China (e-mail: topxdliu@163.com; zh-wang@shou.edu.cn).

Rong Shu is with the Key Laboratory of Space Active Opto-Electronics Technology, Chinese Academy of Sciences (CAS), Shanghai 20083, China, with the Shanghai Institute of Technical Physics CAS, Shanghai 20083, China, and also with the Hangzhou Institute for Advanced Study, UCAS, Hangzhou 310024, China (e-mail: shurong@mail.sitp.ac.cn).

Digital Object Identifier 10.1109/JSTARS.2022.3151332

This work is licensed under a Creative Commons Attribution-NonCommercial-NoDerivatives 4.0 License. For more information, see https://creativecommons.org/licenses/by-nc-nd/4.0/

users can also be extracted from the full-waveform. Land cover classification using data extracted from these remote sensing methods can be utilized by geographers and ecologists to monitor, assess, and understand the ongoing process that drives the geographical changes and identify strategies for sustainable development [1], [13].

For the full-waveform airborne LiDAR, it has been demonstrated that the waveform backscattered coefficient is useful for land cover classification [13]. And many classification experiments using full-waveform data have been established [6], [14], [15]. Mallet *et al.* [16] took a support vector machine (SVM) to mark point clouds according to various scenes and levels of features, and classified building, ground, and vegetation in urban areas with an average accuracy of about 95%. Höfle *et al.* [17] used a decision tree (DT, with $\leq$72% correctness) and an artificial neural network (ANN, with $\leq$95% correctness) by combing raster data and point cloud to analyze the radiometric waveforms about urban vegetation. Ma *et al.* [18] tested a random forest (RF) classifier with features extracted from the waveforms from an airborne LiDAR (LiteMapper 5600), including intensity, distance, full width at half maximum (FWHM), skewness, and kurtosis; and this classifier achieved an accuracy of 89.73% and Kappa of 0.8631, and outperformed SVM in differentiating tree, building, farmland, and ground. However, these methods were performed on the waveform returned from small laser footprint avoided more noise.

For the full-waveform spaceborne laser altimeter, the range from the laser altimeter to the illuminated object, and even more typical characteristic parameters of the target surface and rich vertical structure information can be used into the land-cover classification [19], [20]. For example, the first spaceborne laser satellite [21], geoscience laser altimeter system (GLAS) carried on the ice, cloud, and land elevation satellite (ICESat), launched in January 2003. Besides of the main objective of the GLAS on polar ice-sheet elevation change, atmospheric profiles of cloud and aerosol properties, land topography, and vegetation height [22], [23]. Brenner *et al.* [19] used features, such as the distance between laser and nadir surface, the returned laser pulse energy, and the waveform shape of the GLAS to perform the land-cover classification. In addition, more research has shown that the derived structure information can be used to distinguish the specific land types [20]. Many summary metrics parameters extracted from full-waveform (including number of echoes, total return energy, waveform begin, peak amplitude, echo width, skewness, and kurtosis) have been used to represent the characteristics of the waveforms [1], [11], [16], [21], [24]–[29]. These parameters provide more comprehensive features for the vertical structure of illuminated surface and have been successfully applied to various land types.

In the first period, the vertical structure of the footprint was used as a comprehensive attribution to improve the classification accuracy of remote sensing imagery. Ranson *et al.* [24] conducted an experiment on forest tree species in Siberia using GLAS and MODIS data and showed that GLAS profile information can help understand MODIS land cover categories. Liu *et al.* [30] discriminated land types, including cropland, forest, shrubland, water, and impervious surface, in the laser footprints with RF and SVM, and showed that incorporating GLAS waveform features and Landsat spectra could improve the classification accuracy of footprints and achieved an overall accuracy (OA) of 91%.

In the late period, some supervised machine learning methods were adopted for land cover classification just based on the waveform features. Duong *et al.* [25] tested an example of classification with DT in the Netherlands and clarified five categories (bare land, low vegetation, high vegetation, urban, and water) with an accuracy of approximately 73%. Molijn *et al.* [28] developed a terrain classification on DT with features from GLAS waveform (width, kurtosis, reflectivity, and saturation) to distinguish four land types (snow, ice, rock, and water) with an OA of 74% in the Dry Valleys of Antarctica to estimate the changes in large-scale surface properties on cryosphere. Gong *et al.* [31] estimated the building height and density with GLAS data. Li *et al.* [32], [33] tested a multiclass SVM to classify the GLAS waveforms cover Beijing area into five land types (invalid, plain, building, terraces, and mountain) and achieved an OA of 92.36%. Fayad *et al.* [34] tested the principal component analysis and RF regressions on the canopy height. Zhou *et al.* [1] developed a curve match method based on Kolmogorov–Smirnov distance to classify the waveforms from a relatively level area into three open space categories. Zhao *et al.* [35] compared the classification accuracy of DT and the Gaussian process on the GLAS waveform. However, in the areas covered with dense forests or heterogeneous vegetation, GLAS waveforms are more complex and difficult to be consistently characterized. Generally, the full-waveform can be regarded as a product of the interaction between laser and illuminated area, though it is very sensitive to the surface topography due to the large footprint [36], and this sensitivity becomes more serious in mountainous areas even with complex vegetation cover. There are still existing problems for large number of the waveforms over these areas.

The main objective of this project is to further improve the classification accuracy in differentiating objects with the fine vertical structures based on full-waveform, especially for the mountainous area that is hard to reach. Classifying the land cover of laser footprint based on the returned full-waveform can meet the online classification about the laser spot in a simple and fast way and assess the quality level of laser footprint used as ground control points in the photogrammetry. In this article, we propose an RF-based method for the land cover classification research of GLAS full-waveform data, in where the west-central Yunnan, a south west province in China. The general steps are as follows. First, an improved threshold wavelet procedure is performed to denoise the full-waveform, then Gaussian decomposition method is performed on the denoised waveform to extract the typical characteristic parameters of the object surface and rich vertical structure information. Second, some of the typical feature parameters derived from the decomposition are used to classify land cover, as well as features such as amount of noise, the peak interval, and relative time between peaks. Third, an RF classifier is used to classify the land covers of the mountainous areas into five types: flat land, building, terrace, forest, and mountain. The performances of the RF are compared to other classifiers (such as SVMs with linear and RBF kernel functions, logistic regression (LR), K-nearest neighbor (KNN), and naive Bayes (NB)) using quantitative analysis (producer's accuracy (PA), user's accuracy (UA), OA, precision, recall rate, F1-score, and kappa coefficient). Finally, results and discussion on this experiment are analyzed and summarized.

II. STUDY AREA AND DATASETS

ICESat/GLAS can measure global surface elevation and vegetation. The ICESat operated at an orbit altitude of 600 km with an inclination angle of 94°, and the GLAS instrument used two lasers with green (532 nm) and near-infrared (1064 nm with pulsewidth of 4 nm) wavelength to obtain the vertical profiles of returned energy on a full-waveform at a 40 Hz frequency [22], [37]. From launched in January 2003 to termination in October 2009, it had carried out 19 observation campaigns and collected about two billion waveforms [38]. There were two reference orbits programmed in the operation: one was an 8-day repeat orbit, which acquires the data cover ground calibration sites with enable frequent repeat during the lifetime of Laser 1; the other was a 91-day repeat orbit (with about 33 days subcycle), which provided dense data for scientific usage with Laser 2 and Laser 3 [37]. The direction of laser beam was roughly pointing to nadir (with an approximate 0.3° bias), forming an elliptical spot on the target surface. The diameter of spot was about 70 m, and the spacing of the adjacent spots' center was about 170 m. The average horizontal geolocation accuracy of the footprints was about 3.7 m [20]. There were 15 data products on Level-1 and Level-2 derived from the waveforms, namely GLA01 to GLA15 [39]. These data have been released on the National Snow and Ice Data Center.

A. Study Area

The study area is in the west-central region of Yunnan Province, located in the southwest China, with the longitude approximately of 22°–27° N and the latitude of 99°–102° E. The climate belongs to a subtropical monsoon. The average annual temperature is around 15 °C to 18 °C, and the annual rainfall is approximately 1300–1400 mm. The terrain of Yunnan Province is higher in the northwest and lower in the southeast, showing a gradual downward trend from north to south (Fig. 1). It belongs to mountainous plateau terrain, and the middle altitude area accounts for about 87.21% of the total land area of the province. In terms of terrain types, plain, terrace, hilly, and mountainous areas approximately account for 4.85%, 1.55%, 4.96%, and 88.64%, respectively.

B. Datasets

In the experiment, the waveform data were collected on November 11, 2007, March 17, 2008, and December 13, 2008. GLA01, GLA05, and GLA14 data products were used, where GLA01 contains the transmitted and received waveforms, and the returned waveforms were digitized in 1 ns bin interval and with 544 bins over the land and ice and 200 bins over the oceans and sea ice; GLA05 contains the parameters on the shape of footprints; and GLA14 contains the geographic location and elevation of the footprints. The three data products could be matched by the unique index number and spot number in the header files. As shown in Fig. 1, there are eight ground tracks, and the footprints of the sampling point are determined by the latitude and longitude from GLA14. The experimental dataset includes 1367 waveforms, among which 639 located in the ascending orbit and 728 located in the descending orbit. The data in the red rectangle are missing in natural, as GLAS did not acquire the echo waveforms in this area, while data in the red ovals are sparsely sampled, because data were eliminated when the test requirements were not met.

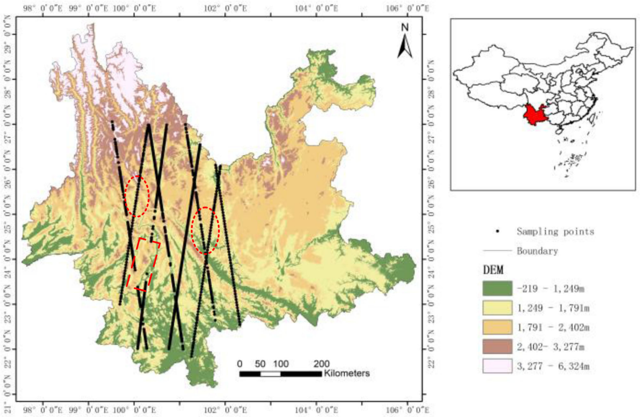

Fig. 1. Study area and eight ICESat/GLAS ground tracks.

The high spatial resolution of Google Earth images has been used as a reliable ground reference in the land cover classification [1], [40]. To minimize the difference and refine the land types, available historical images from Google Earth that closest to the GLAS data time were considered as ground reference. In this article, nearly 3000 high-resolution images (nearly 1 m with eye altitude less than 500 m) released in 2011 or 2013 and 2000 middle-resolution images (almost some meters with eye altitude less than 3000 m) released in 2007 or 2008 were used to compare the GLAS data in 2007 and 2008. The approximate areas of laser footprint could be estimated with the ellipses based on their short and long axes and the orientations of the long axes, which can be derived from the GLA05 product [29]. The GLAS footprints then overlaid on the images, and the land types can be identified with visual interpretation. Additionally, a digital elevation model (DEM) with 30 m spatial resolution and 1° × 1° tiles from ASTER GDEM v3[1] and slope map derived from DEM are also used to analyze the topography of the footprint.

In addition, the coordinate system of all these geographic data is converted to WGS84 used by the Google Earth (with an OA within ±1 m) [41], [42], and then the provincial boundary between them is analyzed to ensure them matching together.

In the study area, there five typical feature types are focused, namely, flat, building, terrace, forest, and mountain. Fig. 2 shows their images, DEMs, slopes, and typical waveforms on the footprints, where the approximate areas are marked with red ellipses

---

[1] [Online]. Available: http://reverb.echo.nasa.gov/reverb/

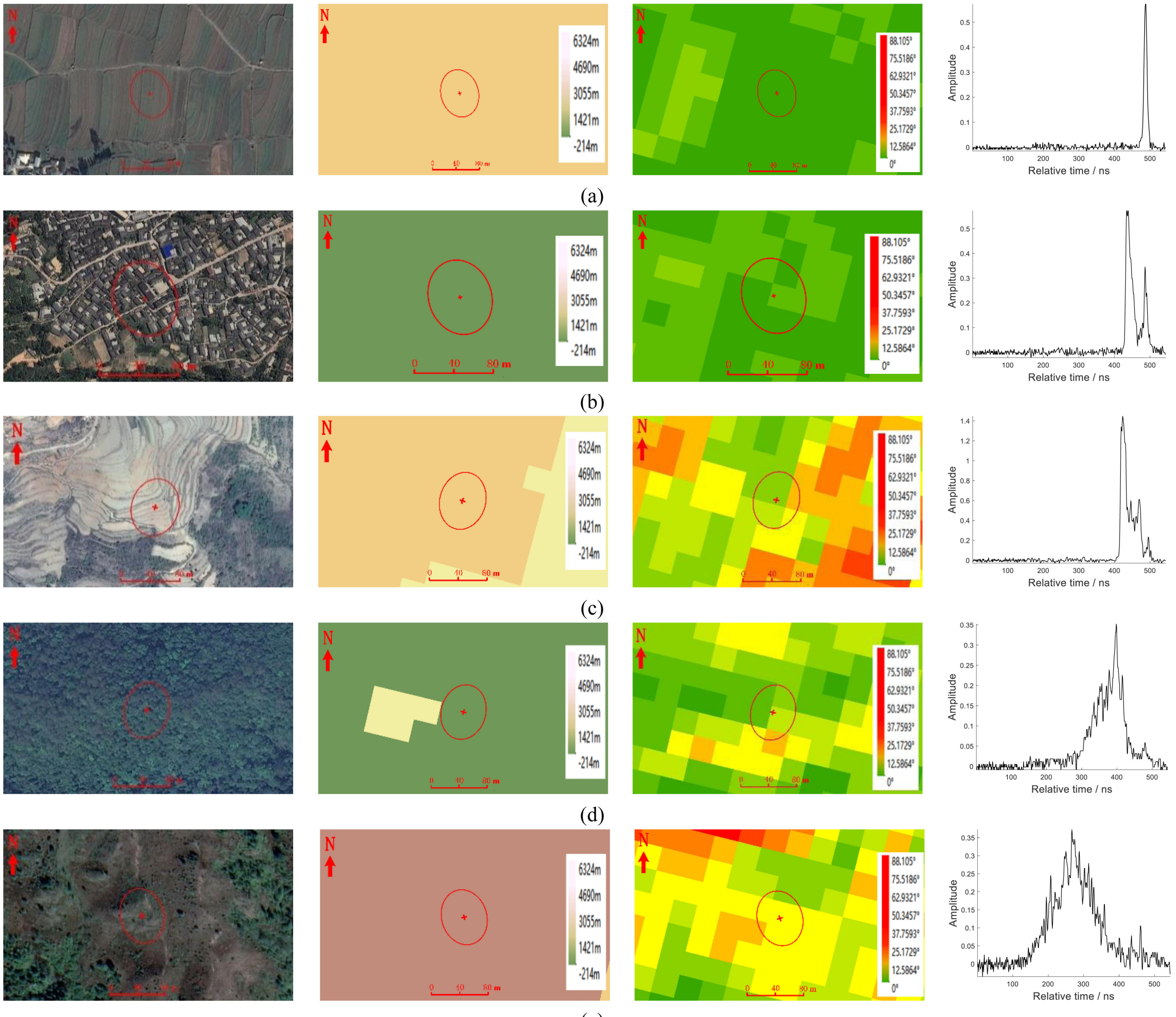

(a)

(b)

(c)

(d)

(e)

Fig. 2. Image, DEM, slope, and GLAS waveform about the five typical land types: (a) flat, (b) building, (c) terrace, (d) forest, and (e) mountain.

(from GLA05) together with the latitude and longitude marked with red crosses (from GLA14). It is difficult to distinguish the mixing of buildings and vegetation from the vegetation just with the waveform, thus the types of mixing of buildings and vegetation are not considered.

Combining the waveform characteristics with the actual scenes of the feature types, a bare or flat land with the open surface mostly gives a single-peak waveform, and the pulsewidth of the return waveform is nearly the same as that of the transmitting pulse. While the wave width of the return waveform increases with the increase of slope gradient and surface roughness. Artificial objects (building and terrace) and vegetation represents complex areas with different height levels, and this will yield overlapping or superimposing Gaussian signals, resulting multipeak and wide-width waveforms. Additionally, roughness surface of artificial objects will introduce more noise into the waveforms. For examples, waveforms over the high vegetation usually have a wider width for the first echo due to the scattering from tree crowns, while waveforms over urban area often have a narrower width for all echoes due to reflectance from the sharp shape of artificial objects. Terraces are flat terrain with a large raised area and low relative height, and the central slope is gentle while the surrounding area is steep. The waveforms on woodland contain information about multiple trees rather than a single tree, and the waveform caused by successive height changes appears to have a high frequency with a larger number of peaks and a wider pulsewidth compared to the flatland waveform. The waveforms returned from hilly or mountainous areas have wider pulsewidth than any other types due to the most complex vegetation and slope gradient.

III. METHODS

A. *Preprocessing of Full-Waveform*

For the ICESat/GLAS, the returned full-waveform is dependent on the transmitted waveform, and can be regarded as the sum of the reflections on distinctive surfaces within laser footprints [43]. Generally, the shape of waveforms is primarily determined by the vertical structures of the dominant land types within the footprint, thus the features of waveform with a dominant land cover type is helpful to identify the corresponding class [1]. To accurately extract the waveform features and classify the land types of footprints, one needs to remove the noise and decompose the waveform beforehand.

1) Noise Reduction: The full-waveform of the spaceborne laser altimetry contains more ground feature information, which can be used as the basic information for the classification of footprints. However, the recorded waveform is always contaminated by various noises, including equipment, environment, object, and others. The noise could be seriously affecting the practical application of the GLAS waveform; thus, it is important to remove the noise first.

Compared to Gaussian filter, wavelet threshold denoising, including wavelet hard or soft threshold and wavelet improved threshold [44]–[46], can effectively retain the main characteristics of the signal. The wavelet coefficients of wavelet hard threshold denoising are discontinuous at the threshold value, and this can produce oscillation when reconstructing the signal. Wavelet soft threshold denoising usually has good continuity, but there is a constant deviation between wavelet coefficients after wavelet decomposition and threshold quantization when the absolute value of the former is greater than the latter, and the loss of edge signal may lead to too smooth and distortion noise reduction. Hence, the following improved wavelet threshold denoising method is adopted:

$$w_n = \begin{cases} \mathrm{sgn}\left(w\right)\left[\dfrac{|w|-aT}{e^{b\left(\frac{|w|-T}{T}\right)}}\right], \ |w| \geq T \\ 0, \ |w| < T \end{cases} \tag{1}$$

where a and b are the adjustment factors and $a \in [0,1], b > 0$. The improved wavelet threshold becomes the wavelet hard threshold when $a = 0$ and the soft threshold when $a = 1$ and $b = 0$. The improved wavelet threshold combines the benefits of both hard and soft threshold, and the proper selection of parameters can achieve the best effect of wavelet threshold.

2) Normalization: Considering the influence of measure environment and instrument itself during the laser pulse transmission, the returned energy of waveform usually has more variations. The normalization of waveform data could be conducted to yield a unified standard, and this further helps to improve the retrieval accuracy of the data and ensures the reliability of waveform feature extraction. It is assumed that wave has only finite real values, normalizing the minimum and maximum values to $y_{\min}$ and $y_{\max}$, which is expressed as follows:

$$y = \frac{\left(y_{\max} - y_{\min}\right)\left(x - x_{\min}\right)}{x_{\max} - x_{\min}} + y_{\min} \tag{2}$$

where x is the original values and y is the normalized values.

3) Waveform Decomposition: The returned full-waveform contains more detailed characteristics in the footprint of illuminated object. Decomposing the full-waveform can obtain typical characteristic parameters and rich vertical structure information. At present, the most widely used waveform decomposition methods include wavelet decomposition [47], Gauss decomposition [9], [48], and deconvolution decomposition [49], [50]. Among them, the wavelet method requires the prespecification of wavelet basis function, decomposition scale, and threshold value, and these requirements limit its application; and the deconvolution method has stricter requirements on noise reduction and inherits some other certain ill-conditioned problems. The transmitted pulse of the laser is considered to follow the Gaussian distribution, so does to the returned waveform of complex object, which is the result of superposition of Gaussian pulses reflected by multiple single objects [51], it also considered to follow as the Gaussian distribution. As a result, the complex returned full-waveform can be decomposed into multiple Gaussian components and represented as follows [1]:

$$w\ (t) = \sum_{m=1}^{N} w_m\left(t\right) = \sum_{m=1}^{N} A_m e^{\frac{-(t-t_m)^2}{2\sigma_m^2}} \tag{3}$$

where $w(t)$ is a denoised and normalized waveform, $w_m(t)$ is the amplitude of individual components at the time of t, $N$is the number of Gaussian components, and A_m, t_m, and σ_m are the amplitude, peak position, and pulsewidth of the individual components, respectively.

In the procedure of Gaussian decomposition, the peak of the waveform components can be detected by the parity inflection point method, and then the parameters of waveform features can be determined, for example pulsewidth, amplitude, peaks' number, peaks' position, and so on. For the parity inflection point method, the first derivative is regarded as peak position and the amplitude of the peak can be derived from the waveform; the second derivative is the inflection point position, and the width of the components can be calculated with the second derivative and first derivative; the pulsewidth is the closest value from the inflection point to the peak position; and the peak value is the maximum value between adjacent odd and even inflection points. The number of the Gaussian components can be counted, and generally counts to six Gaussian components for the complex GLAS full-waveform. When the number of waveform components decomposed out is larger than 6, the combination will be conducted according to the principle of pulsewidth and peak area [20]. More components parameters can be determined after the nonlinear curve fitting of waveform can be solved with the Levenberg–Marquardt [7]. The local noise is calculated with a standard deviation on the first 150 bins of the raw waveform, and the global noise is meant the local noise of the entire waveform. Meanwhile, a threshold value of each waveform can be set as the maximum value of local noise, and this threshold value can be used to truncate the waveform by specifying the actual begin and end positions [25]. Therefrom, the beginning of waveform is the intersection of the horizontal threshold line with the first rising edge of the waveform, and the end of waveform is the last intersection, here regarded as the beginning and end of waveform. The width of waveform is the distance between the beginning and the end positions of the waveform. The peak position is usually taken as the component location, and the flying time can be used to calculate the range from laser transmitter to the target [10]. Intensity, which can be simply expressed in the term of the echo amplitude, is the combination of emitted energy, distance, atmosphere attenuation, and reflection of illuminated target [52]. FWHM represents the extension of waveform in the incident direction, and it is closely related to the geometry and topographic slope of target [7]. Skewness of returned waveform indicates the degree of asymmetry of a distribution around its mean value, and kurtosis of returned measures the relative peakedness and flatness of a distribution [19]. In brief, the main feature parameters can be extracted from the Gaussian decomposition algorithm, and can be used in the next classification to distinguish the typical land types.

B. Classification Based on Waveform Features

Varieties of nonparametric classifiers have been introduced, e.g., ANN, DT, and SVM. In this article, the RF classifier is demonstrated under the complex environments. We also compared its performance with the other classifiers, for example, linear-SVM and radial basis function SVM (RBF-SVM) [53], LR [54], KNN [55], and NB [56]. And the quantitative analysis is also evaluated.

1) Random Forest Classifier: RF is a versatile supervised machine learning algorithm that combines multiple DTs to reach a single result [57]. RF uses bagging and feature randomness to create low correlated DTs. The construction of each DT in the forest relies on an independent randomly selected training set. There is no strong dependency between DTs, and multiple DTs can be generated in parallel. To ensure low correlation among DTs, only a subset of possible features to instead of all features will be used to construct the DT split. The RF algorithm has four main hyperparameters: the number of trees (*n*_estimators), the division criteria of nodes (criterions), the leaf node size, and the number of features sampled. This algorithm also introduces two random selection methods during construction process: one is that the training set is randomly selected by bootstrap method; and the other one is that split features are randomly selected from the candidate features.

It is usually trained with bagging method to combine multiple machine learning models to improve the overall performance. The structure of DT is a tree: each internal node indicates a test of an attribute, each branch represents a prediction result, and each leaf node represents a category. When a DT is used to classify a sample test set, it is necessary to start from the root node: detect the corresponding features of the test set samples according to the features represented by nonleaf nodes, select branches according to the output results, assign the test samples to its subnodes until completely classified into leaf nodes, and the category represented by the leaf node will be the classification result of the test sample.

The RF algorithm is consisted of a set of DTs, and each tree in the ensemble is comprised of a data sample extracted from a training set with replacement, as known as bootstrap sample. For the training samples, half of them is set as test data, named as out-of-bag sample, and will be sued at later. Another instance of randomness is then injected through feature bagging to increase the diversity of the dataset and reduce the correlation between DTs. The overall prediction depends on the outcome type: for a regression task, the individual DTs usually could be averaged; and for the classification task, the predicted classes are generated by majority voting on the most frequent categorical variables. Finally, the out-of-bag sample is used for cross-validation and to estimate the final prediction. In the DTs, Gini index or information entropy (IE) is usually used as the selection metric. The information gain (4) can be used as the feature selection, where IE (5) of the dataset *T* represents the purity of these sample data, and the feature that minimizes the IE of the dataset should be selected as the split feature. If *Q* is selected as the split feature the dataset *T*, as (6)

$$\text{Gain }(Q) = \text{IE}\,(T) - \text{IE}_Q\,(T) \tag{4}$$

$$\text{IE }(T) = -\sum_{i\,=\,1}^{m} p_i \log_2 p_i \tag{5}$$

$$\text{IE}_Q\ (T) = \sum_{j=1}^{k} \frac{|T_j|}{|T|}\,\text{IE}\,(T_j) \tag{6}$$

where *m* is the number of categories contained in the dataset *T*, p_i is the proportion of samples with category *i* in the dataset *T*; *k* is the splitting of dataset *T* into *k* copies using the split feature *Q*, and T_j is the *j*th copy of the dataset obtained by splitting. It can be seen from the equation that the closer the proportions of samples of different categories in the dataset, the greater IE and larger number of categories.

2) Training and Validation Samples: In the RF procedure, a training dataset from reference waveforms is needed to create the model, which is used to predict future outcomes. And the training and testing samples are usually divided by random sampling within each category. The extracted waveform features (including the number of Gaussian components, the waveform pulsewidth, the amount of noise, the relative time between peaks, and the beginning and end of waveform) for each sample are used to classify the land types. And the class labels of samples are obtained by selecting the main object or an object cluster based on the geolocation and the high-resolution Google Earth images that are within approximate areas of the laser footprint and close to the waveform acquisition time, due to the horizontal geolocation errors (average with 3.7 m) of the GLAS data [20], [58]. Meanwhile, the topography is also used to assist in the analysis. In this article, the RF-based classification is performed in two phases: 1) the training phase, where the extracted features and related class labels are used to train a classifier; and 2) the testing section, where each waveform is assigned to the class that has the closest similarity with the reference waveform.

As shown in the Fig. 3, the specific process of RF-based classification generally have the following five steps: 1) use the

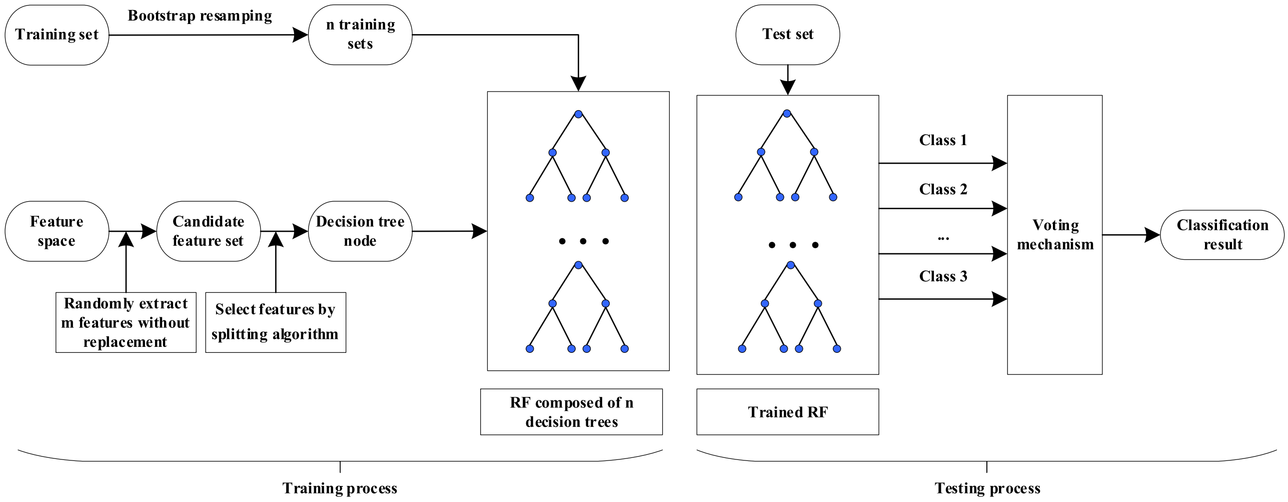

Fig. 3. Training and validation procedures of the random forest.

bootstrap method to extract samples from the replaced training samples as the training set of the DT, and use the unextracted samples as the out-of-bag data; 2) repeat the above steps many times to get the training set and out-of-bag data; 3) use the obtained multiple training sets to build a DT, for each node of the DT, randomly extract *m* features from the feature space as the candidate feature set; 4) select the optimal feature from the candidate feature set according to the information gain as the split feature to generate a DT, the generated multiple DTs form an RF; and 5) input the test sample into the trained RF model. Each DT in the RF will vote on the classification result, and the class with the most votes is the final classification class of the test sample.

3) Accuracy Assessment: The performances of RF and other classifiers are assessed and compared with PA, UA, OA, accuracy, precision, recall rate, F1-score, and kappa coefficient, and these indexes are calculated using testing samples in this article as follows:

a) PA corresponds to error of omission and indicates the percentage of correctly classified class samples among the true class in the test set. It indicates the degree of classification of the reference data for this category, and expressed as follows:

$$\text{PA} = \frac{a_{ii}}{\sum_{i=1}^{N} a_{ji}} \tag{7}$$

where *N* is the number of categories of feature types,a_{ii} is the number of correctly classified samples, and a_{ji} is the total number of samples of class *j* divided into class *i*.

b) UA corresponds to error of commission and represents the percentage between the number of samples correctly classified in the test set and the total number of samples in this category in the test set

$$\text{UA} = \frac{a_{ii}}{\sum_{i=1}^{N} a_{ij}} \tag{8}$$

where $a_{ij}$is the total number of samples of class *i* divided into class *j*.

c) OA refers to the probability that the classification result for each random sample is consistent with the actual result. It is calculated as the total number of correctly classified samples divided by the reference samples, and can be expressed as

$$\text{Accuracy} = \frac{\text{TP} + \text{TN}}{\text{TP} + \text{TN} + \text{FP} + \text{FN}}. \tag{9}$$

d) The precision represents the proportion of true positive samples among those predicted positive samples, and can be expressed as

$$\text{Precision} = \frac{\text{TP}}{\text{TP} + \text{FP}}. \tag{10}$$

e) The recall represents the proportion of true positive sample among those actual positive sample, and can be expressed as

$$\text{Recall} = \frac{\text{TP}}{\text{TP} + \text{FN}}. \tag{11}$$

f) As the accuracy and recall are used as the evaluation results, the index measurement is prone to saturation. Therefore, F1-score is used as the evaluation standard, which can be expressed as

$$\text{F1} - \text{score} = \frac{2 \times \text{Precision} \times \text{Recall}}{\text{Precision} + \text{Recall}} \tag{12}$$

where TP is the number of positive classes predicted to be positive classes, TN is the number of negative classes predicted to be negative classes, FP is the number of negative classes predicted to be positive classes, and FN is the number of positive classes predicted to be negative classes.

g) The kappa coefficient is usually used to test the spatial consistency of image classification. It is an index to measure the classification accuracy. The higher the kappa coefficient, the higher the classification accuracy of the

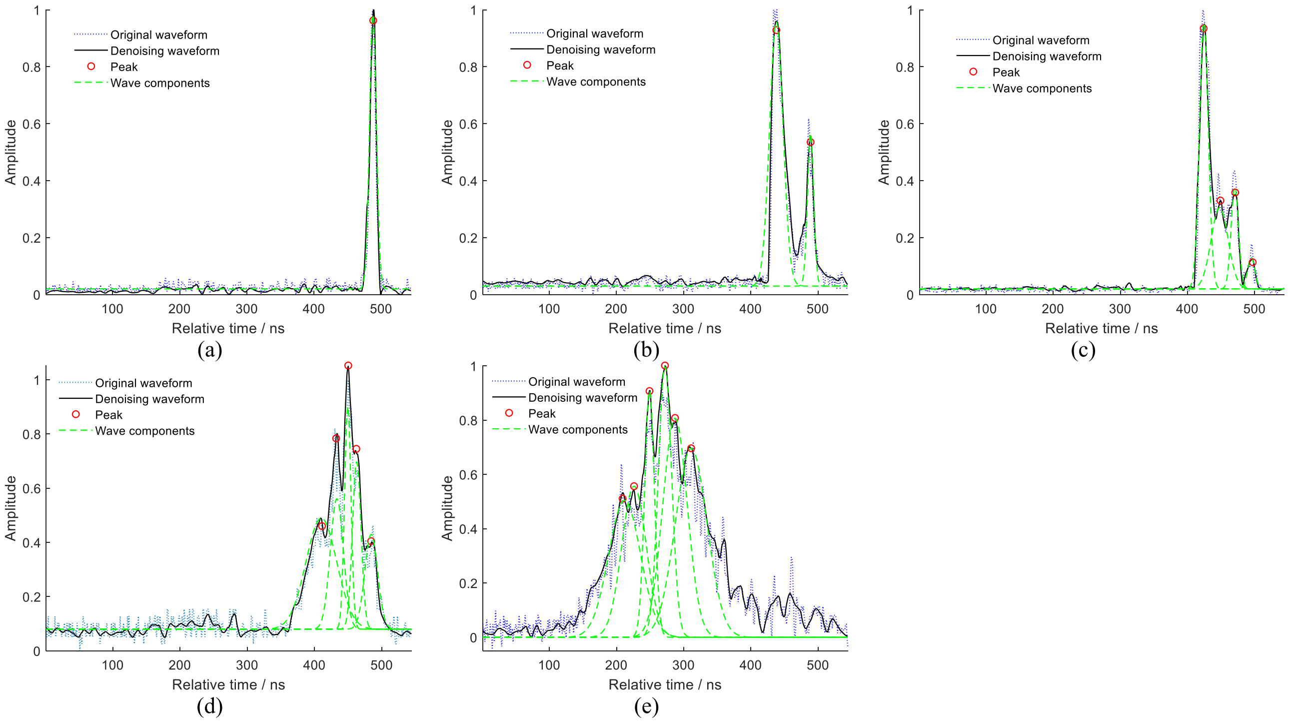

(a) (b) (c) (d) (e)

Fig. 4. Normalization, noise reduction, and decomposition of five typical full-waveforms: (a) flat, (b) building, (c) terrace, (d) forest, and (e) mountain.

model which can express as follows:

$$\text{kappa} = \frac{\text{Accuracy} - p_1}{1 - p_1} \tag{13}$$

where

$$p_1 = \frac{a_1 \times b_1 + a_2 \times b_2 + \cdots + a_n \times b_n}{n \times n} \tag{14}$$

and $a_1, a_2, \cdots, a_n$ indicates the number of actual samples of each type, $b_1, b_2, \cdots, b_n$ indicates the number of prediction samples for each type, and n is the total number of samples.

IV. RESULTS AND DISCUSSION

A. *Pretreatments of Full-Waveform*

In the experiment, a total of 1367 full-waveforms were selected from GLA01, in this study area, including 269 flat waveforms, 217 building waveforms, 213 terrace waveforms, 440 forest waveforms, and 228 mountain waveforms. The original full-waveform was normalized to make the full-waveform form different ground object processed and analyzed under a unified standard. The improved wavelet threshold denoising was first used to reduce the noise on the normalized full-waveforms. The threshold parameter was determined by unbiased risk estimation criterion with the wavelet basis function db4 and the level 3. The Gaussian decomposition was finally conducted on pretreated full-waveform into one or up to six Gaussian components. And then the typical characteristic parameters were extracted to distinguish different types of footprints.

Fig. 4 shows the pretreatments of GLAS full-waveform, including normalization, noise reduction, and decomposition. In this figure, blue dotted line and black solid line represent the normalized and denoising waveform on the five types. The Gaussian white noise in the waveform is eliminated and denoised, and the number and position of the main peaks (marked with the red circle) in the waveform are retained after the noise reduction. The full-waveform usually consists of one or more echoes, one echo may correspond to an individual target or an object cluster too close to be separated, while multiple echoes usually represent multiple targets or a target with multiple vertically separable components in the footprint [6]. The wave component about echoes represents with green dotted line. Consequently, features of the full-waveform will be directly related to the land cover types. Fig. 4(a) shows the waveform over a flat surface, which displays a single peak with a narrow width nearly the same as the transmitted pulsewidth, meaning a high concentration of energy returned almost simultaneously. There will be a spread in the pulse and a decrease in the amplitude when the surface slope is greater than 10° [36]. There is no significant influence on the waveform shape about majority of the flat surfaces, in this article. Fig. 4(b) shows the waveform over a building area, which displays an obvious interval between the two relatively independent wave peaks, and the amplitude of the first peak is higher than the second one. The waveform is mainly determined by the combined influence of the height and vertical structure of building, as well as the percentage of area covered by building in the footprint. When the building is high enough, the peak interval of the returned pulse can be distinguished easily from the ground surface. Fig. 4(c) shows the waveform over some terraces, which displays multiple peaks close to each other, and the amplitude of the first peak is higher than others. The height difference of the terraces is much smaller than that of the buildings and

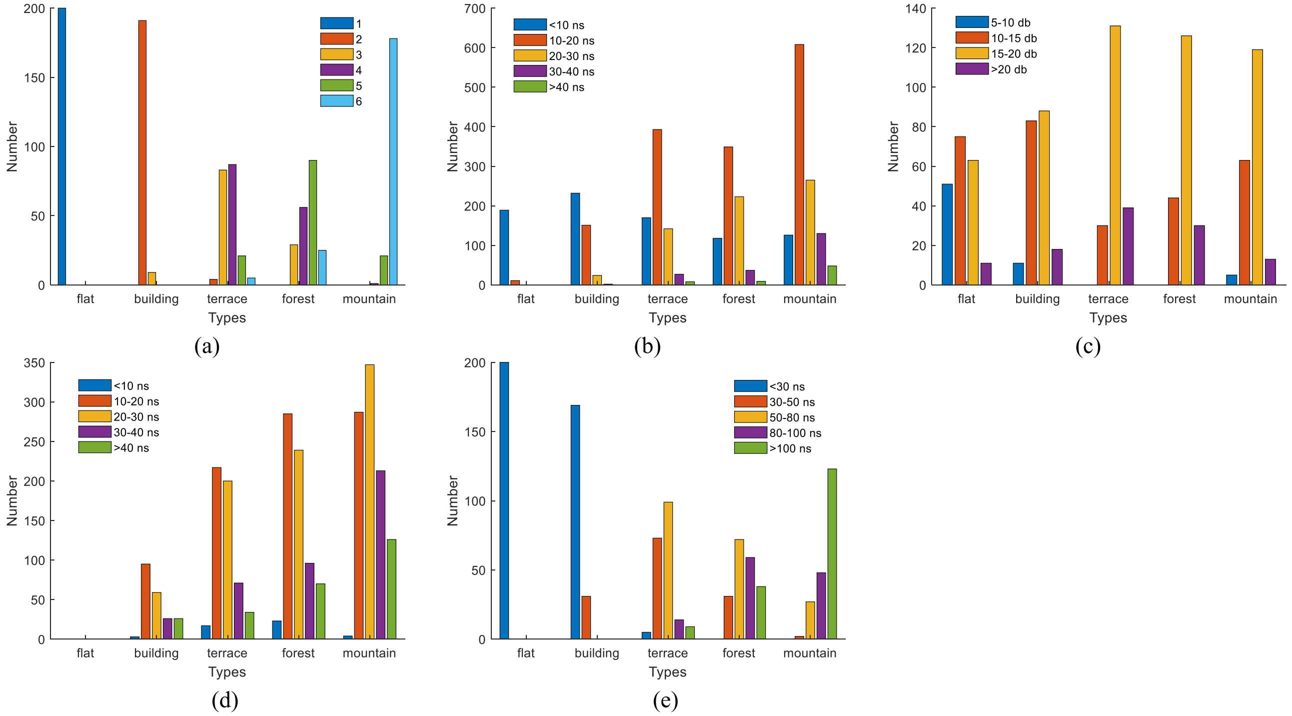

(a) (b) (c) (d) (e)

Fig. 5. Details of each waveform characteristic parameter in the sample set: (a) number of Gaussian components, (b) waveform pulsewidth, (c) amount of noise, (d) relative time between peaks, and (e) begin and end of waveform.

the interval between peaks is less obvious. This is because the terrace terrain is close to a flat or a gently sloping landform surface. Fig. 4(d) shows the waveform over forest. There are some specific features about forest waveforms, for example, the pulsewidth spread due to multireflection echo from vegetation, the high frequency due to the consecutive height variation, and greater influence of global noise by the rough surfaces, compared to the flat. For the large footprint, the waveform over forest contains more information over the forest canopy and multiple forest elements than individual trees, and it is derived from the density, structure, and vegetation phase of tress. Fig. 4(e) shows the waveform over mountain. It has larger expansion than other types due to various sloping and roughness on a large scale. Overall, the last echo waveform decomposed is the ground echo for all land types; the amplitude of first echo on the building and terrace is largest in all peaks, compared to those on forest and mountain, and the waveform noise is relatively larger on the forest and mountain than that on the building and terrace.

Many characteristic parameters extracted from the Gaussian components can be used to classify different land covers. To analyze the intrinsic relationship between these characteristic parameters and the land types, there 200 samples from each of the five types were selected and counted in the experiment. Fig. 5 shows the five main features on these land covers analyze with the 1000 samples, such as the number of Gaussian components, the pulsewidth of waveform, the global noise, the relative time between peaks, and the beginning and end of waveform. To the best of our knowledge, two characteristic parameters on the global noise and the relative time between peaks are never used as classification criteria by previous article. The noise represents the surface roughness of the object and can be used to discriminate the buildings' floor, flat with grass, and plain; and the relative time between peaks indicates the actual distance between multiple features in the laser footprint.

Fig. 5(a) shows the number of Gaussian components on the five land types. It is obviously that the flat waveforms have only one component; nearly all the building waveforms have two components, and few have three; most terrace waveforms have two or three components, some have five, and few have six; half of forest waveforms have five components, some have four, and the others have three and six; nearly all of mountain waveforms have six components, and a few have five. Fig. 5(b) shows the pulsewidth of the waveforms on the five land types. It is clearly that nearly all flat waveforms have pulsewidth less than 10 ns with a few between 10 and 20 ns; most of building waveforms distribute in the range of less than 10, some between 10 and 20 ns, and a few between 20 to 30 ns; while most mountain waveforms have pulsewidth between 10 and 20 ns. It also observes the numbers of bin with width 10 to 20 ns and with 20 to 30 ns gradually increases across the five land types. Fig. 5(c) shows the global noise contained in the waveforms on the five land types. Mountain, forest, and terrace waveforms have the highest noise level, followed by the building and flat. And terrace shows a relatively high noise because it may be overbounded in vegetation. Fig. 5(d) denotes the relative distance between the peaks of Gaussian components. Since the flat waveforms consist of only a single peak, this feature parameter does not exist and is set to zero in the dataset. The mountain waveforms have the most varied waveform pulsewidth due to the slope and ground roughness, so the relative distance between their

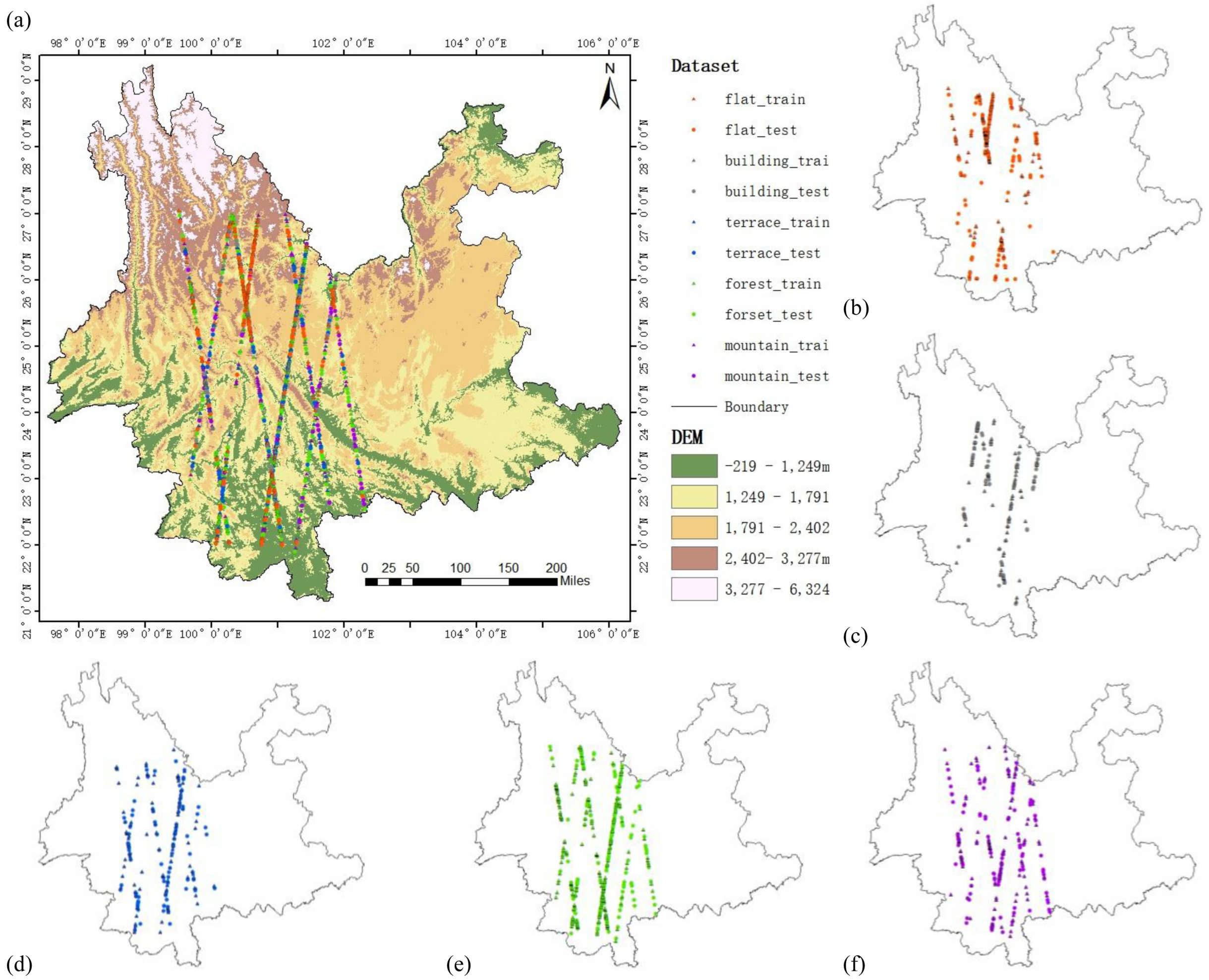

Fig. 6. Classification results of the laser footprints: (a) all samples, (b) flat, (b) building, (d) terrace, (e) forest, and (f) mountain.

peaks is the largest. The relative distance between the peaks of the building waveform is larger compared to that of the terrace waveform, which means that the actual distance between buildings in the actual terrain is larger than the actual distance between each terrace level. Fig. 5(e) shows the beginning and end of waveforms on the five land types. Since the flat land is the farthest from the laser pulse emitter, the transmission time of the laser pulse is the longest when acquiring the waveform, resulting the late beginning position. The mountain waveforms are greatly influenced by the terrain topography and vegetation, so their begin position is the earliest and end position is the latest; followed by the forest waveforms, which are influenced by the change of tree height, and their beginning position is earlier than the terrace waveforms and the building waveforms; the terrace waveforms are obtained from the terrace, and their beginning position is earlier compared with those of the building.

B. *Classification and Comparison*

Generally, a single Gaussian component is used in this article to distinguish flat waveforms, and the waveform width of flat is narrower than other land types. The distance between peaks is used to distinguish between buildings and terraces, since the peak relative distance of terrace waveforms is smaller than that of the buildings. The beginning of waveform is used to distinguish between buildings and forests, where the wave beginning position of forests is usually earlier. The pulsewidth of waveform is used to distinguish between forests and mountains because the mountain waveforms are influenced by slope gradient and surface roughness, and the pulsewidths are wider than other land types. The amount of noise is used to distinguish between terraces and forests because the forest waveform contains information of a variety of trees, and the high frequency of the waveform caused by continuous height change introduces noise signal, while the central slope of the terrace is gentle and has less noise signal.

In the experiment, the scikit-learn, an open-source machine learning library in Python, is used for the classification based on waveforms' feature. Half of the samples were randomly selected and set as the training set, and the remaining samples were set as the testing set. The training set is the class labels in the original sample set corresponding to the test set. In which, there are a total of 683 feature attributes of waveforms in the training set, and the waveforms to which the feature attributes belong include

TABLE I
EVALUATION INDEX OF CLASSIFICATION RESULTS OF EACH CLASSIFIER

Methods	Land types	PA(%)	UA(%)	OA(%)	Precision(%)	Recall(%)	F1-score(%)	Kappa
Linear-SVM	Flat	100.00	100.00	90.35	90.34	91.58	90.90	0.8764
	Building	97.22	99.05					
	Terrace	82.20	87.38					
	Forest	89.09	82.81					
	Mountain	83.18	88.67					
RBF-SVM	Flat	100.00	100.00	93.12	93.20	93.81	93.43	0.9117
	Building	98.13	99.05					
	Terrace	87.50	81.98					
	Forest	91.40	88.98					
	Mountain	88.98	93.05					
LR	Flat	100.00	100.00	95.32	95.23	95.77	95.44	0.9399
	Building	97.22	99.05					
	Terrace	94.28	89.18					
	Forest	95.02	92.51					
	Mountain	89.65	98.11					
KNN	Flat	99.25	100.00	87.13	87.51	88.11	87.70	0.8347
	Building	97.19	98.11					
	Terrace	77.00	69.36					
	Forest	82.43	80.61					
	Mountain	81.66	92.45					
NB	Flat	100.00	100.00	83.45	82.55	82.98	81.16	0.7765
	Building	61.27	100.00					
	Terrace	74.67	47.74					
	Forest	88.88	77.53					
	Mountain	84.96	86.62					
RF	Flat	100.00	100.00	97.95	97.73	98.30	97.99	0.9737
	Building	98.14	100.00					
	Terrace	97.24	95.49					
	Forest	98.64	96.03					
	Mountain	94.64	100.00					

135 flats, 111 buildings, 102 terraces, 213 forests, and 122 mountains, respectively; and a total of 684 feature attributes of waveforms in the test set, and the waveforms to which the feature attributes belong include 134 flats, 106 buildings, 111 terraces, 227 forests, and 106 mountains, respectively. Fig. 6 shows the classification results of the training and testing samples on the five land types. The distribution of land types is generally reasonable, and consistent with the land cover of Yunnan Province.

To perform and evaluate this method on the classification, there are other methods simultaneously conducted, such as linear-SVM, RBF-SVM, LR, KNN, and NB. The quantitative analysis of these methods is conducted with seven terms, as shown in Table I.

From the perspective of PA and UA on the five land types, all the six methods can classify the flat land perfectly. For the other four land types, all the methods do very well on the building and forest, but performed the worst on terrace with the worst result. The RF method also performed the best on the other four land types, with PA and UA of 98.14% and 100.00%, 97.24% and 95.49%, 98.64% and 96.03%, and 94.64% and 100.00% on the building, terrace, forest, and mountain, respectively. However, the NB method performed the worst among all the methods on building, terrace, forest, and mountain, with PA and UA of 61.27% and 100.00%, 74.67% and 47.74%, 88.88% and 77.53%, and 84.96% and 86.62%, respectively. In the classification procedure, there are more misclassifications on building, terrace, forest, and mountain. The misclassification between buildings and terraces may be the result of indeterminate threshold of the relative time between peaks; and the misclassification of forests and mountains is usually observed in the case of dense forests and sparse mountains, because they share large similarities between the extracted parameters on the begin of the waveform and the waveform pulsewidth. In addition, the lower classification accuracy of buildings and forests is due to the potential for confounding between the two types or mixing of them. It is difficult to distinguish forests from those in montane areas, and this may cause the lowest classification accuracy of mountain.

For the perspective of OA, precision, recall, F1-score, and kappa coefficient on these methods, the RF classifier has the best performances on the classification in the all of land covers, with the OA, precision, recall, F1-score, and kappa of 97.95%, 97.73%, 98.30%, 97.99%, and 0.9739, respectively. The NB classifier performed the lowest, with the accuracy of them is 83.45%, 82.55%, 82.98%, 81.16%, and 0.7765, respectively. And then LR classifier performed better than RBF-SVM, linear-SVM, and KNN, with the accuracy of them is 95.32%, 95.23%, 95.77%, 95.44%, and 0.9399, respectively. For the hyperparameters of RandomForestClassifier in sklearn, the larger *n*_estimators in the RF model, the better of the performance, which was achieved at the expense of higher memory occupied usage and longer training time. In the experiment, when *n*_estimators = 10 by default, the classification accuracy rate was 97.95%; and when it was adjusted to 17, the accuracy rate reached the highest as 97.99% and the kappa coefficient was 0.9737. In the classification of flat land and building, the classification is completely correct. For the testing set on the terrace waveforms, one was classified as building, and another one was classified as the forest. For the testing set on the forest waveforms, four of them were misclassified as mountain. In the classification of LR, there twenty forest waveforms were divided into mountain, seven mountain waveforms were categorized as forest waveforms, and seven terrace waveforms were mistakenly classified as forest or building. The classification precision of linear-SVM and RBF-SVM is 90.34% and 93.20%, and the kappa coefficient is 0.8764 and 0.9117, respectively. The classification effect of RBF-SVM is slightly better than linear-SVM because the former performs better in linear nonseparable scenarios. The KNN classifier performed slightly better than NB, but the selection of the value is a big problem for KNN classifier, and this will influence the results. In the experiment of NB, nearly half of terrace waveforms were classified as building, about 22.47% of forest waveforms were incorrectly classified, and about 10.38% of mountain waveforms were classified as forest. Although RF method performs the best performances on the classification in the five land types, there is still a certain dependence on the training samples.

V. CONCLUSION

Full-waveform spaceborne laser altimeter has an ability of observing the earth almost all the time, helps to derive more vertical structure information about the land cover at global scale. And classifying the land cover of laser footprint based on the returned full-waveform can meet the online classification in a simple and fast way and assess the quality level of laser footprint used as the ground control points in photogrammetry. However, it is very sensitive to surface topography, even with the complex vegetation in mountainous regions. It is still existing problems occurring for large number of the waveforms over these areas.

To further improve the classification accuracy based on full-waveform alone to differentiate objects with fine vertical structures. In this project, it proposes an improved method based on RF for the land cover classification research of GLAS full-waveform data, in where the west-central Yunnan, a southwest Chinese province. First, an improved threshold wavelet procedure is performed to denoise the GLAS full-waveform, then a Gaussian decomposition is used to extract the waveforms' characteristic parameters, such as the number of Gaussian components, the pulsewidth, the global noise, the relative time between peaks, and the beginning and end of waveform. Second, an RF algorithm is conducted and compared with other methods, such as linear-SVM, RBF-SVM, LR, KNN, and NB. They are implemented to classify the waveforms on five types: flat land, building, terrace, forest, and mountain. And the quantitative analysis of classification accuracy is indicated with PA, UA, OA, precision, recall rate, F1-score, and kappa coefficient. And the results show that all the six methods can accurately classify the flat land, with the PA and UA achieve to 100.00%. The method of RF has the best performances in other four land types with the PA and UA of 98.14% and 100.00%, 97.24% and 95.49%, 98.64% and 96.03%, and 94.64% and 100.00%, respectively. And the OA, precision, recall, F1-score, and kappa coefficient for the RF are 97.95%, 97.73%, 98.30%, 97.99%, and 0.9737, respectively, while 83.45%, 82.55%, 82.98%, 81.16%, and 0.7765 for NB, which has the worst performance. The LR performed better than RBF-SVM, linear-SVM, and KNN. We also observe worse classification accuracy for all methods when the waveforms are more complex.

The classification demonstrates the potential of classifying the land types within laser footprint based on full-waveform. It is conducted here an RF algorithm using GLAS waveform to improve the classification accuracy in differentiating objects with the fine vertical structures. Our future article will extend the footprint classification to the Global Ecosystem Dynamics Investigation laser data and China's Gaofen-7 laser altimeter.

ACKNOWLEDGMENT

The authors would like to thank the National Snow and Ice Data Center for providing ICESat/GLAS data and ASTER GDEM data from NASA, and the Google Earth for releasing high resolution images. The authors also would like to thank all the anonymous reviewers for their constructive suggestion to improve the quality of this article.

REFERENCES

[1] Y. Zhou, F. Qiu, A. A. Al-Dosari, and M. S. Alfarhan, "ICESat waveform-based land-cover classification using a curve matching approach," *Int. J. Remote Sens.*, vol. 36, no. 1, pp. 36–60, Jan. 2015, doi: 10.1080/01431161.2014.990648.

[2] H. Buddenbaum, S. Seeling, and J. Hill, "Fusion of fullwaveform LiDAR and imaging spectroscopy remote sensing data for the characterization of forest stands," *Int. J. Remote Sens.*, vol. 34, no. 13, pp. 4511–4524, Apr. 2013, doi: 10.1080/01431161.2013.776721.

[3] Z. Qi, A. G. Yeh, X. Li, and Z. Lin, "A novel algorithm for land use and land cover classification using RADARSAT-2 polarimetric SAR data," *Remote Sens. Environ.*, vol. 118, pp. 21–39, Mar. 2012, doi: 10.1016/j.rse.2011.11.001.

[4] S. Uhlmann and S. Kiranyaz, "Classification of dual- and single polarized SAR images by incorporating visual features," *ISPRS J. Photogramm. Remote Sens.*, vol. 90, pp. 10–22, Apr. 2014, doi: 10.1016/j.isprsjprs.2010.05.002.

[5] A. C. Brenner, J. P. DiMarzio, and H. J. Zwally, "Precision and accuracy of satellite radar and laser altimeter data over the continental ice sheets," *IEEE Trans. Geosci. Remote Sens.*, vol. 45, no. 2, pp. 321–331, Feb. 2007, doi: 10.1109/TGRS.2006.887172.

[6] C. Alexander, K. Tansey, J. Kaduk, D. Holland, and N. J. Tate, "Backscatter coefficient as an attribute for the classification of full-waveform airborne laser scanning data in urban areas," *ISPRS J. Photogramm. Remote Sens.*, vol. 65, no. 5, pp. 423–432, Sep. 2010, doi: 10.1016/j.isprsjprs.2010.05.002.

[7] V. H. Duong, "Processing and application of ICESat large footprint full waveform laser range data," Ph.D. dissertation, Aerosp. Eng., Delft Univ. Technol., Delft, The Netherlands, 2010.

[8] T. Sasaki, J. Imanishi, K. Ioki, Y. Morimoto, and K. Kitada, "Object-based classification of land cover and tree species by integrating airborne LiDAR and high spatial resolution imagery data," *Landscape Ecol. Eng.*, vol. 8, no. 2, pp. 157–171, Jul. 2012, doi: 10.1007/s11355-011-0158-z.

[9] W. Wagner, A. Ullrich, V. Ducic, T. Melzer, and N. Studnicka, “Gaussian decomposition and calibration of a novel small-footprint full-waveform digitising airborne laser scanner,” *ISPRS J. Photogramm. Remote Sens.*, vol. 60, no. 2, pp. 100–112, Apr. 2016, doi: 10.1016/j.isprsjprs.2005.12.001.

[10] C. Mallet and F. Bretar, “Full-waveform topographic lidar: State-of-the-art,” *ISPRS J. Photogramm. Remote Sens.*, vol. 64, no. 1, pp. 1–16, Jan. 2009, doi: 10.1016/j.isprsjprs.2008.09.007.

[11] J. Zhang, A. de Gier, Y. Xing, and G. Sohn, “Full waveform-based analysis for forest type information derivation from large footprint spaceborne LiDAR data,” *Photogramm. Eng. Remote Sens.*, vol. 77, no. 3, pp. 281–290, Mar. 2011, doi: 10.14358/PERS.77.3.281.

[12] V. Ussyshkin and L. Theriault, “Airborne lidar: Advances in discrete return technology for 3D vegetation mapping,” *Remote Sens.*, vol. 3, no. 12, pp. 416–434, Dec. 2011, doi: 10.3390/rs3030416.

[13] W. Y. Yan, A. Shaker, and N. El-Ashmawy, “Urban land cover classification using airborne LiDAR data: A review,” *Remote Sens. Environ.*, vol. 158, pp. 416–434, Mar. 2015, doi: 10.1016/j.rse.2014.11.001.

[14] V. Ducic, M. Hollaus, A. Ullrich, W. Wagner, and T. Melzer, “3D vegetation mapping and classification using full-waveform laser scanning,” in *Proc. Workshop 3D Remote Sens. Forestry*, Feb. 2006, pp. 211–217.

[15] C. Mallet, U. Soergel, and F. Bretar, “Analysis of full-waveform liDAR data for classification of urban areas,” *Int. Arch. Photogramm., Remote Sens. Spatial Inf. Sci.*, vol. XXXVII, pp. 85–91, 2008.

[16] C. Mallet, F. Bretar, M. Roux, U. Soergel, and C. Heipke, “Relevance assessment of full-waveform lidar data for urban area classification,” *ISPRS J. Photogramm. Remote Sens.*, vol. 66, no. 6, pp. S71–S84, Dec. 2011, doi: 10.1016/j.isprsjprs.2011.09.008.

[17] B. Höfle, M. Hollaus, and J. Hagenauer, “Urban vegetation detection using radiometrically calibrated small-footprint full-waveform airborne LiDAR data,” *ISPRS J. Photogramm. Remote Sens.*, vol. 67, no. 1, pp. 134–147, Jan. 2012, doi: 10.1016/j.isprsjprs.2011.12.003.

[18] L. Ma, M. Zhou, and C. Li, “Land covers classification based on random forest method using features from full-waveform LiDAR data,” in *Proc. Int. Arch. Photogramm., Remote Sens. Spatial Inf. Sci.*, 2017, pp. 263–268.

[19] A. C. Brenner *et al.*, *Derivation of Range and Range Distributions From Laser Pulse Waveform Analysis for Surface Elevations, Roughness, Slope and Vegetation Heights*, Algorithm Theoretical Basis Document, Version 4.1. Greenbelt, MD, USA: NASA Goddard Space Flight Center, 2003.

[20] X. Wang, X. Chen, P. Gong, H. Huang, Z. Li, and X. Li, “Earth science applications of ICESat/GLAS: A review,” *Int. J. Remote Sens.*, vol. 32, no. 23, pp. 8837–8864, Dec. 2011, doi: 10.1080/01431161.2010.547533.

[21] H. Wu and Y. Xing, “Comparison between ETM+ imageries and ICESat-GLAS waveforms for forest classification,” in *Proc. 2nd Int. Conf. Inf. Sci. Eng.*, Dec. 4–6, 2010, pp. 1088–1092.

[22] H. J. Zwally *et al.*, “ICESat’s laser measurements of polar ice, atmosphere, ocean, and land,” *J. Geodyn.*, vol. 34, no. 3/4, pp. 405–445, Oct. 2002, doi: 10.1016/S0264-3707(02)00042-X.

[23] V. H. Duong, R. Lindenbergh, N. Pfeifer, and G. Vosselman, “Single and two epoch analysis of ICESat full waveform data over forested areas,” *Int. J. Remote Sens.*, vol. 29, no. 5, pp. 1453–1473, Mar. 2008, doi: 10.1080/01431160701736372.

[24] K. J. Ranson, G. Sun, K. Kovacs, and V. I. Kharuk, “Landcover attributes from ICESat GLAS data in central Siberia,” in *Proc. IEEE Int. Conf. Geosci. Remote Sens. Symp.*, 2004, pp. 753–756, doi: 10.1109/IGARSS.2004.1368511.

[25] H. Duong, N. Pfeifer, and R. Lindenbergh, “Full waveform analysis: ICESat laser data for land cover classification,” in *Proc. ISPRS Commission VII Mid-Term Symp. Remote Sens., Pixels Processes*, May 8–11, 2006, pp. 30–35.

[26] R. Narayanan, H. B. Kim, and G. Sohn, “Classification of SHOALS 3000 bathymetric LiDAR signals using decision tree and ensemble techniques,” in *Proc. IEEE Toronto Int. Conf.–Sci. Technol. Humanity*, Sep. 26–27, 2009, pp. 462–467.

[27] P. Zaletnyik, S. Laky, and C. Toth, “LIDAR waveform classification using self-organizing map,” in *Proc. Amer. Soc. Photogramm. Remote Sens. Annu. Conf.*, Apr. 26–30, 2010, pp. 1055–1066.

[28] R. A. Molijn, R. C. Lindenbergh, and B. C. Gunter, “ICESat laser full waveform analysis for the classification of land cover types over the cryosphere,” *Int. J. Remote Sens.*, vol. 32, no. 23, pp. 8799–8822, Dec. 2011, doi: 10.1080/01431161.2010.547532.

[29] X. Wang *et al.*, “Lake water footprint identification from time-series ICESat/GLAS data,” *IEEE Geosci. Remote. Sens. Lett.*, vol. 9, no. 3, pp. 333–337, May 2012, doi: 10.1109/LGRS.2011.2167495.

[30] C. Liu *et al.*, “Joint use of ICESat/GLAS and landsat data in land cover classification: A case study in Henan Province, China,” *IEEE J. Sel. Topics Appl. Earth Observ. Remote Sens.*, vol. 8, no. 2, pp. 511–522, Feb. 2015, doi: 10.1109/JSTARS.2014.2327032.

[31] P. Gong, Z. Li, H. Huang, G. Sun, and L. Wang, “ICEsat GLAS data for urban environment monitoring,” *IEEE Trans. Geosci. Remote Sens.*, vol. 49, no. 3, pp. 1158–1172, Mar. 2011, doi: 10.1109/TGRS.2010.2070514.

[32] X. Li, L. Ma, and L. Xu, “Land classification from LiDAR full-waveforms based on multi-class support vector machines,” in *Proc. IEEE Int. Conf. Imag. Syst. Techn.*, Oct. 2013, pp. 1–6.

[33] X. Li, L. Ma, and L. Xu, “Real-time terrain classification using ICESat/GLAS data over Beijing area,” *Remote Sens. Lett.*, vol. 5, no. 7, pp. 591–600, Jul. 2015, doi: 10.1080/2150704X.2014.942922.

[34] I. Fayad *et al.*, “Canopy height estimation in French Guiana with LiDAR ICESat/GLAS data using principal component analysis and random forest regressions,” *Remote Sens.*, vol. 6, no. 12, pp. 11883–11914, Dec. 2014, doi: 10.3390/rs61211883.

[35] Q. Zhao, X. Li, and L. Xu, “Comparison of two approaches for land cover classification from ICESat/GLAS waveform data,” in *Proc. IEEE Int. Conf. Imag. Syst. Techn.*, Oct. 2017, pp. 1–6.

[36] C. Hilbert and C. Schmullius, “Influence of surface topography on ICESat/GLAS forest height estimation and waveform shape,” *Remote Sens.*, vol. 4, no. 8, pp. 2210–2235, Jul. 2012, doi: 10.3390/rs4082210.

[37] B. E. Schutz, H. J. Zwally, C. A. Shuman, D. Hancock, and J. P. Dimarzio, “Overview of the ICESat mission,” *Geophys. Res. Lett.*, vol. 32, no. 21, pp. S01–S04, Nov. 2005, doi: 10.1029/2005GL02400.

[38] R. Nelson, “Model effects on GLAS-based regional estimates of forest biomass and carbon,” *Int. J. Remote Sens.*, vol. 31, no. 5, pp. 17–19, Oct. 2008, doi: 10.1080/01431160903380557.

[39] L. C. Brittingham and J. Lee, “GLAS standard data products specification–level 2 version 8,” May 2010. [Online]. Available: http://glas.wff.nasa.gov/files/documents/gsas_prod_spec_2_v8.pdf

[40] E. H. Helmer, M. A. Lefsky, and D. A. Roberts, “Biomass accumulation rates of amazonian secondary forest and biomass of old-growth forests from landsat time series and the geoscience laser altimeter system,” *J. Appl. Remote. Sens.*, vol. 3, Dec. 2009, Art. no. 033202, doi: 10.1117/1.3082116.

[41] N. Z. Mohammed, A. Ghazi, and H. E. Mustafa, “Positional accuracy testing of Google Earth,” *Int. J. Multidisciplinary Sci. Eng.*, vol. 4, no. 6, pp. 6–9, Jul. 2013.

[42] M. A. Goudarzi and R. J. Landry, “Assessing horizontal positional accuracy of Google Earth imagery in the city of Montreal, Canada,” *Geodesy Cartogr.*, vol. 43, no. 2, pp. 56–65, Jun. 2017, doi: 10.3846/20296991.2017.1330767.

[43] B. Blair and M. Hofton, “Modeling laser altimeter return waveforms over complex vegetation using high-resolution elevation data,” *Geophys. Res. Lett.*, vol. 26, no. 16, pp. 2509–2512, Jan. 1999, doi: 10.1029/1999GL010484.

[44] D. Donoho, “Denoising by soft thresholding,” *IEEE Trans. Inf. Theory*, vol. 41, no. 3, pp. 613–627, May 1995, doi: 10.1109/18.382009.

[45] D. Donoho and I. M. Johnstone, “Adapting to unknown smoothness via wavelet shringkage,” *J. Amer. Statist. Assoc.*, vol. 90, no. 432, pp. 1200–1224, Dec. 1995.

[46] Z. Huang *et al.*, “Image denoising based on the dyadic wavelet transform and improved threshold,” *Multiresolution Inf. Process.*, vol. 7, no. 3, pp. 4–7, 2009.

[47] C. Wang, F. Tang, L. Li, G. Li, F. Cheng, and X. Xi, “Wavelet analysis for ICESat/GLAS waveform decomposition and its application in average tree height estimation,” *IEEE Geosci. Remote. Sens. Lett.*, vol. 10, no. 1, pp. 115–119, Jan. 2013, doi: 10.1109/LGRS.2012.2194692.

[48] Y. Xing *et al.*, “An improved method for estimating forest canopy height using ICESat/GLAS full waveform data over sloping terrain: A case study in Changbai mountains, China,” *Int. J. Appl. Earth Observ. Geoinf.*, vol. 12, no. 5, pp. 385–392, Oct. 2010, doi: 10.1016/j.jag.2010.04.010.

[49] A. L. Neuenschwander, “Evaluation of waveform deconvolution and decomposition retrieval algorithms for ICESat/GLAS data,” *Can. J. Remote. Sens.*, vol. 34, pp. S240–S246, Jun. 2014, doi: 10.5589/m08-044.

[50] T. Zhou, S. C. Popescu, K. Krause, R. D. Sheridan, and E. Putman, “Gold—A novel deconvolution algorithm with optimization for waveform LiDAR processing,” *ISPRS J. Photogramm. Remote Sens.*, vol. 129, pp. 131–150, Jul. 2017, doi: 10.1016/j.isprsjprs.2017.04.021.

[51] M. A. Hofton, J. B. Minster, and J. B. Blair, “Decomposition of laser altimeter waveforms,” *IEEE Trans. Geosci. Remote Sens.*, vol. 38, no. 4, pp. 1989–1996, Jul. 2000, doi: 10.1109/36.851780.

[52] W. Wagner, J. Hyyppä, A. Ullrich, H. Lehner, C. Briese, and S. Kaasalainen, "Radiometric calibration of full-waveform small-footprint airborne laser scanners," *Int. Arch. Photogramm. Remote Sens. Spatial Inf. Sci.*, vol. XXXVII, no. Pt B1, pp. 163–168, 2008.

[53] M. Zhou, C. Li, L. Ma, and H. Guan, "Land cover classification from full-waveform lidar data based on support vector machines," *Int. Arch. Photogramm. Remote Sens. Spatial Inf. Sci.*, vol. XLI-B3, pp. 447–452, 2016, [Online]. Available: https://doi.org/10.5194/isprs-archives-XLI-B3-447-2016

[54] Y. K. Qawqzeh, A. S. Bajahzar, M. Jemmali, M. M. Otoom, and A. Thaljaoui, "Classification of diabetes using photoplethysmogram (PPG) waveform analysis: Logistic regression modeling," *Biomed. Res. Int.*, vol. 2020, no. 4, pp. 1–6, Aug. 2020, doi: 10.1155/2020/3764653.

[55] D. Zhang, W. Zuo, Y. Li, and N. Li, "Pulse waveform classification using ERP-based difference-weighted KNN classifier," in *Proc. Int. Conf. Med. Biometrics*, 2010, pp. 191–200, [Online]. Available: https://doi.org/10.1007/978-3-642-13923-9_20

[56] X. D. Zhu, J. S. Su, Q. F. Wu, and H. Dong, "Naive Bayes classification algorithm based on optimized training data," *Adv. Mater. Res.*, vol. 490-495, pp. 460–464, Mar. 2012, [Online]. Available: https://doi.org/10.4028/www.scientific.net/AMR.490-495.460

[57] L. Breiman, "Random forests," *Mach. Learn.*, vol. 45, pp. 5–32, Oct. 2001, [Online]. Available: https://doi.org/10.1023/A:1010933404324

[58] T. J. Urban, B. E. Schutz, and A. L. Neuenschwander, "A survey of ICESat coastal altimetry applications: Continental coast, open ocean island, and inland river," *Terr. Atmos. Ocean. Sci.*, vol. 19, no. 1/2, pp. 1–19, Apr. 2008, doi: 10.3319/TAO.2008.19.1-2.1(SA).

Xiangfeng Liu received the B.S. degree in geographic information system from Information Engineering University, Zhengzhou, China, in 2008, the M.S. degree in cartography and geographic information engineering from Liaoning Technical University, Fuxin, China, in 2011, and the Ph.D. degree in cartography and geographic information engineering from Tongji University, Shanghai, China, in 2017.

He is currently a Research Assistant with the Shanghai Institute of Technical Physics, Chinese Academy of Sciences, Shanghai, China. His research interests include calibration and application of active and passive remote sensing.

Xiaodan Liu received the B.S. degree in software engineering from Qufu Normal University, Weifang, China, in 2019. She is currently working toward the M.S. degree in computer technology at Shanghai Ocean University, Shanghai, China.

Her research interests include processing and application of spaceborne laser altimeter.

Zhenhua Wang received the B.S. degree in geographical science from School of Geographical Sciences, Yantai Normal University, Yantai, China, in 2004, the M.S. degree in geochemistry from Chinese Academy of Sciences, Beijing, China, in 2007, and the Ph.D. degree in cartography and geographic information engineering from Tongji University, Shanghai, China, in 2010.

She is currently an Associate Professor with the College of information technology, Shanghai Ocean University, Shanghai, China. Her research interests include spatial data analysis, data quality control, and deep learning.

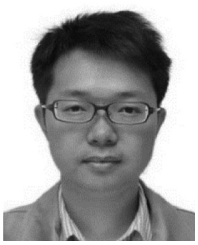

Genghua Huang received the B.S. degree in mechanical engineering from Tsinghua University, Beijing, China, in 2002, and the Ph.D. degree in physical electronics from the Chinese Academy of Sciences, Shanghai, China, in 2007.

He is currently a Senior Researcher with the Shanghai Institute of Technical Physics, CAS, Shanghai, China. His research interests include spaceborne laser altimeter and LIDAR.

Dr. Huang is the Director Designer of the laser rangefinder of Chang'e-3 Lunar exploration lander, and Gaofen-7 laser altimeter system. He was elected as excellent young scientist of program of youth innovation promotion association, CAS, top notch talent of Shanghai. He was the recipient of grants of outstanding contributions of Chang'e-3 exploration task, etc.

Rong Shu received the B.S. degree in mechanical and electrical integration from the Hefei University of Technology, Hefei, China, in 1992, and the Ph.D. degree in physical electronics from the Graduate School of the Chinese Academy of Sciences, Shanghai, China, in 2006.

He is currently a Senior Researcher with the Shanghai Institute of Technical Physics, CAS, Shanghai, China. His research interests include space active opto-electronics technology.

Dr. Shu has led the payload development tasks in a number of national major space missions, such as lunar exploration missions, Tianwen-1 Mars mission, high-resolution earth observation system projects, and so on. He also served as the Deputy Director of China's first quantum scientific experiment satellite (Mozi Satellite). He has been the recipient of more than ten national and provincial awards, as well as an International Award, i.e., 2018 Cleveland Prize.